CrossMark

RESEARCH ARTICLE

An experimental investigation on the surface water transport process over an airfoil by using a digital image projection technique

Kai Zhang[1] · Tian Wei[1,2] · Hui Hu[1]

Abstract In the present study, an experimental investigation was conducted to characterize the transient behavior of the surface water film and rivulet flows driven by boundary layer airflows over a NACA0012 airfoil in order to elucidate underlying physics of the important micro-physical processes pertinent to aircraft icing phenomena. A digital image projection (DIP) technique was developed to quantitatively measure the film thickness distribution of the surface water film/rivulet flows over the airfoil at different test conditions. The time-resolved DIP measurements reveal that micro-sized water droplets carried by the oncoming airflow impinged onto the airfoil surface, mainly in the region near the airfoil leading edge. After impingement, the water droplets formed thin water film that runs back over the airfoil surface, driven by the boundary layer airflow. As the water film advanced downstream, the contact line was found to bugle locally and developed into isolated water rivulets further downstream. The front lobes of the rivulets quickly advanced along the airfoil and then shed from the airfoil trailing edge, resulting in isolated water transport channels over the airfoil surface. The water channels were responsible for transporting the water mass impinging at the airfoil leading edge. Additionally, the transition location of the surface water transport process from film flows to rivulet flows was found to occur further upstream with increasing velocity of the oncoming airflow. The thickness of the water film/rivulet flows was found to increase monotonically with the increasing distance away from the airfoil leading edge. The runback velocity of the water rivulets was found to increase rapidly with the increasing airflow velocity, while the rivulet width and the gap between the neighboring rivulets decreased as the airflow velocity increased.

1 Introduction

Icing is widely recognized as one of the most serious weather hazards to aircraft operations. Aircraft icing occurs when small, super-cooled, airborne water droplets, which make up clouds and fog, freeze upon impact with a surface, which results in the formation of ice (Mason 1971). The freezing can be complete or partial, depending on how rapidly the latent heat of fusion can be released into the ambient air. In a dry regime, all the water collected in the impingement area freezes on impact to form rime ice. For a wet regime, only a fraction of the collected water freezes in the impingement area, while the remaining water runs back and can freeze outside the impingement area to form *glaze ice* (Politovich 1989; Hu and Huang 2009; Hu and Jin 2010). Because of its wet nature, glaze ice can form much more complicated shapes, which are very difficult to accurately predict, and the resulting ice shapes tend to substantially deform the accreting surface with the formation of "horns" and larger "feathers" growing outward into the airflow (Vargas and Tsao 2007). Glaze ice is considered as the most dangerous type of ice. Glaze ice formation can severely decrease the airfoil aerodynamic performance by causing large-scale flow separations that produce dramatic increases in drag and decreases in lift (Politovich 1989; Gent et al. 2000).

The transport behavior of unfrozen water prior to freezing has a direct impact on the shape of glaze ice because it

✉ Hui Hu
huhui@iastate.edu

1 Department of Aerospace Engineering, Iowa State University, Ames, IA 50010, USA

2 School of Aeronautics and Astronautics, Shanghai Jiao Tong University, Shanghai 200240, China

redistributes the impinging water mass. Current ice accretion models usually ignore the complicated details of the interactions between the unfrozen surface water, the ice, the local airflow, the ice phase transition due to the lack of knowledge about the micro-physical phenomena. The surface water transport and surface roughness are usually treated in a simplistic or heuristic manner, typically using correlations or simple decoupled models (Hansman and Turnock 1989; Otta and Rothmayer 2009). Simplistic evaluation of surface roughness and surface water transport behavior that neglects the surface physics is considered to be a significant factor in the poor agreement between the predictions of the glaze ice accretion models and experimental measurements of glaze ice (Hansman and Turnock 1989; Myers and Charpin 2004; Brakel et al. 2007).

Advancing technology for safe and efficient aircraft operation in atmospheric icing conditions requires a better understanding of the important micro-physical phenomena pertinent to aircraft icing phenomena. While several studies have been carried out to investigate the impacts of various types and amounts of ice accreted on aircraft wings (either through icing wind tunnel testing or using "artificial" iced profiles) on the aerodynamic performances of iced airfoils/wings (Bragg et al. 1986; Koomullila et al. 2003), very few studies focused on the fundamental micro-physical processes associated with aircraft icing phenomena. As a result, many important micro-physical processes (e.g., transient behavior of surface water film/rivulet flows; interactions between the surface water, the local airflow, and ice; unsteady heat transfer within water droplets and film flows; or freezing process of water flows over smooth and rough ice surfaces) are still unclear (Otta and Rothmayer 2009; Hu and Huang 2009; Hu and Jin 2010). Advanced experimental techniques, which are capable of providing accurate, quantitative measurements to quantify the micro-physical processes pertinent to aircraft icing phenomena, are highly desirable. In the present study, we report the progress made in our recent efforts to develop a novel digital image projection (DIP) system to achieve non-intrusive, temporally resolved, full-field thickness measurements of the water film and rivulet flows on airfoil surfaces to quantify the surface water transport process pertinent to aircraft icing phenomena.

In the sections that follow, the technical basis of the DIP technique is briefly described; the feasibility, accuracy, and implementation of the DIP technique are demonstrated by measuring the profile of a small spherical cap over a test plate to evaluate the measurement accuracy level of the DIP system; the DIP system is then applied to measure time-resolved thickness distributions of unsteady water film and rivulet flows over a NACA0012 airfoil; finally, we summarize the conclusions of the study.

2 Technical basis of digital image projection (DIP) technique

2.1 Literature review of the experimental techniques for water film flow measurements

Several experimental techniques have been developed in recent years to achieve quantitative, non-intrusive film thickness distribution measurements of surface water film/rivulet flows, including fluorescence imaging techniques, density-based techniques, stereoscopic imaging techniques, and image correlation-based techniques. The technical basis and applications of the measurement techniques are briefly reviewed in this section. We also comment on the advantages and the limitations of these techniques for icing physics studies.

Laser-induced fluorescence (LIF) is a technique widely used for qualitative flow visualizations and quantitative measurements of passive scalar distributions in fluid flows. In particular, fluorescence imaging techniques have been used to conduct film thickness measurements of surface film/rivulet flows. According to quantum theory (Pringsheim 1949), for a diluted solution and unsaturated excitation, the acquired fluorescence intensity will be a function of the number of fluorescent tracer molecules and fluid temperature. With the reasonable assumption of uniformly distributed tracer molecules throughout a thin film, the local film thickness is proportional to the number of the tracer molecules in the line of sight of an image detector. Hence, the thickness distribution of the thin film can be derived from the acquired fluorescence images if the fluid flow is under isothermal condition or the temperature distribution of the fluid flow is known. Several studies have been conducted using fluorescence imaging techniques to measure the thickness distributions of thin film flows. For example, Liu et al. (1995) conducted an experiment to quantify the dynamic thickness variations of film flows due to gravity-driven instabilities using the fluorescence imaging technique. Johnson et al. (1997, 1999) developed a fluorescence imaging system to quantify the transient behavior of thin film flows over flat surfaces under isothermal conditions. Essentially, the same fluorescence imaging approach has also been used by Lel et al. (2005), Chinnov et al. (2007), and Schagen and Modigell (2007) for film thickness measurements under various experimental settings. It should be noted that transparent fluids are required to use fluorescence imaging techniques for film thickness measurements. In an icing environment, however, water film and rivulet flows over an icing surface may become semitransparent or even opaque. Furthermore, LIF intensity is usually temperature dependent, and the temperature of the surface water film and rivulet flows varies significantly during the icing

process. As a result, it would be very difficult, if not impossible, to use the fluorescence imaging technique to conduct quantitative film thickness measurements of water film and rivulet flows in an icing environment.

A density-based color light encoding technique was developed by Zhang et al. (1996) to measure free-surface gradients of fluid flows, and this method was successfully applied to measure the surface deformation due to near-surface turbulence. For these measurements, an array of lenses transformed the rays of a light source into a series of color-coded parallel light beams by passing the light through a group of color palettes at the focal planes of the lens array. The parallel light beams were used to illuminate a free surface of water. The reflected rays from the free surface were captured by a charge-coupled device (CCD) color camera above the surface. The slopes were derived from the color images after calibration, and surface elevations were obtained by integrating the slopes. Other density-based approaches include diffusing light photography (Wright et al. 1996), which was employed to investigate the free-surface motion, and Schlieren techniques, which were used to qualitatively visualize the liquid–gas interface instabilities of a locally heated falling liquid film (Kabov et al. 2002). It will be quite difficult, if not impossible, to use the density-based approaches to achieve accurate thickness distribution measurements of water film and rivulet flows over icing surfaces because the change of the index of refraction at the water–ice interface and the thermally induced density changes in the water film and rivulet flows significantly affect the measurement results.

A three-dimensional (3D) binocular stereogrammetry system (called wave acquisition stereo system) was developed by Benetazzo (2006) to recover topographic information from overlapping video sequences captured by two synchronized cameras. Image analysis techniques were used for retrieving water surface elevation fields spatially and temporally from the acquired image sequences. A remarkable feature of the stereo imaging method is its capability to measure surface discontinuities (Tsubaki and Fujita 2005). The measurable length scales were found to depend on the pixel resolution, the triangulation accuracy, and the acquisition frame rate. The accuracy of the technique depends on the geometry of the stereo rig and the camera resolution. The distance between the cameras and the inclination angle of the cameras' lines of sight was also found to strongly affect the measurement uncertainty. The measurement performance rapidly degrades with increasing distance between the cameras and the water surface.

More recently, Moisy et al. (2007) developed a non-intrusive optical method for the measurement of the instantaneous interface between two transparent fluids. This method is based on the analysis of the refracted image of a random dot pattern visualized through the interface. The apparent displacement field between the refracted image and a reference image was determined using a digital image correlation (DIC) algorithm. The main limitations of the method are: (1) it is unable to detect changes in the mean surface height, (2) it is extremely sensitive to slight vibrations, (3) it is unable to determine the displacement field for strong curvature and/or large surface-pattern distance. The limitations are usually unacceptable for accurate thickness distribution measurements of water film and rivulet flows in icing physics studies.

Another category of measurement technique capable of achieving non-intrusive thickness measurements in film flows is the structured light technique. This technique relies on actively projecting known light patterns onto an object, and extracting 3D surface shapes from the images of the light pattern captured from one or more points of view (Salvi et al. 2010). Structured light techniques have been applied very successfully in many fields, including 3D sensing, object recognition, robotic control, industrial inspection of manufactured parts, stress/strain and vibration measurements, biometrics, biomedicine, dressmaking, and visual media. Structured light techniques are also receiving the attention of the fluid dynamics community in recent years. For example, Cazabat et al. (1990) used a technique to project equally spaced fringes to reconstruct the thickness profiles of thin spreading films to investigate the characteristics of climbing film flows driven by temperature gradients. Zhang and Su (2002) applied a fringe projection technique to reconstruct vortex shapes at a free surface. Pouliquen and Forterre (2002) employed essentially the same method to record the time evolution of free-surface deformations of dense granular flow. Cochard and Ancey (2008) designed a digital fringe projection system to measure the time evolution of the dam-break surge downstream from an inclined plate. Cobelli et al. (2009) conducted an experiment using a digital fringe projection system to measure the surface deformations of a water flow. More recently, Hu et al. (2014) developed a digital fringe projection (DFP) system to quantify the transient behavior of wind-driven water droplet and rivulet flows over a flat test plate. The DFP described in Hu et al. (2014) relies on projection of a digital fringe pattern with the light intensity varying sinusoidally across the fringe pattern onto the surface of a 3D object to be measured. The projected fringe pattern would be modulated by the 3D object placed on a reference plane. Fourier transform method is used for DFP image processing to determine the phase maps for the modulated pattern and the reference images. A rather complicated phase unwrapping process is also needed in order to calculate the phase changes between the modulated fringe pattern and the reference image correctly. Finally, by using a phase-to-height conversion relationship determined through a calibration procedure, the 3D profile of the test

object with respect to the reference plane is retrieved based on the measured phase changes between the modulated fringe pattern and the reference image. However, since the DFP technique is assumed that the fringe pattern recorded by the sensor is a signal with spatial carrier frequencies modulated in both phase and amplitude in order to use Fourier transformation method to reconstructed the phase maps of the acquired modulated pattern and reference images, the imperfection of the projected digital fringe pattern, i.e., the acquired image intensity of the digital fringe pattern may not vary perfectly in a sinusoidal function as assumed, may cause significant measurement errors in the DFP measurements, as reported in Zhang et al. (2013). While the DIP technique to be introduced in the present paper is also a structured light technique that relies on actively projecting known light patterns onto an object in order to extract 3D surface shapes of the object from the acquired image of the projected image pattern, the DIP technique offers great advantages over the DFP technique described in Hu et al. (2014) with a better flexibility in selecting of the desirable patterns for image projection, much simpler image processing methods to extract 3D surface shapes of the measured object from the acquired images, and a higher measurement accuracy in the measurement results.

2.2 The technical basis of the DIP technique

While the DIP technique is similar to a stereo-based imaging method, it uses a projector to replace one of the cameras needed for stereo-based imaging (Salvi et al. 2010). Figure 1 shows the schematic of a typical DIP system. A digital projector is used to project image patterns of known characteristics onto a test object of interest (e.g., the water film and rivulet flows over a test surface in the present study). Due to the complex surface shape of the test object, the projected image patterns will be deformed when observed from a different perspective than the projection
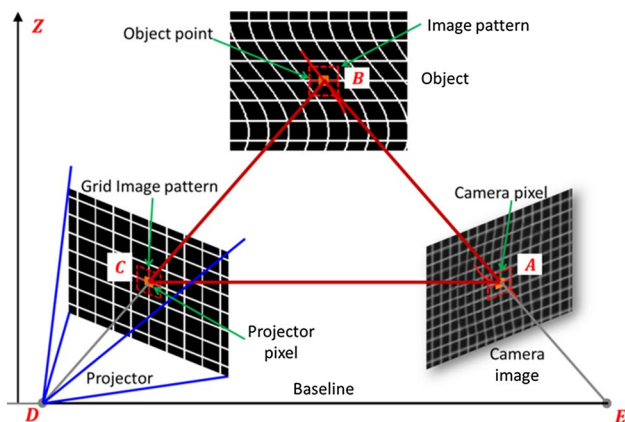

Fig. 1 Schematic of DIP technique

axis. The projection unit (*D*), image acquisition unit (*E*), and the three-dimensional object (*B*) form a triangulation base. If the corresponding points between the camera (*A*) and the projector (*C*) are identified through a calibration procedure, the 3D shape of a test object can be obtained through an analysis of the triangulation of *ΔABC*.

For the DIP technique introduced here, the correspondence is established by finding the displacement vectors between corresponding points in the distorted images (i.e., the images acquired with the water film/rivulet flows on the test surface) and a reference image (i.e., the image acquired without the water film/rivulet flows on the test surface). More specifically, by determining the displacement vectors at the points of interests between the modulated images and the reference image using a cross-correlation image processing algorithm, the 3D shape of the test object of interest with respect to the reference surface (i.e., the thickness distribution of the water film/rivulet flows on the test surface) can be determined quantitatively and instantaneously.

2.2.1 Displacement to height conversion for DIP measurements

As described above, the deformation of the projected image patterns observed by the camera contains the height information of the measured object (i.e., the shape of the water film/rivulet flows over an airfoil surface for the present study); thus, the 3D shape of the measured object can be restructured based on the displacement map of the corresponding points between the distorted images and the reference image, if the DIP system is calibrated properly. To convert the displacement map to a height distribution, the relationship between the height and the displacement must be established. Figure 2 shows the diagram of the DIP technique for displacement to height conversion. A reference plane with a height 0 in the Z-direction is used as the reference surface for all subsequent measurements. The arbitrary point "M" in the captured image corresponds to point "N" in the projected image, and point "D" on the object surface. From the projector's point of view, point "D" on the object surface has the same position as point "A" on the reference plane. However, from the point of view of the image recording camera, point "D" on the object surface images will be at the same position as the point "C" on the reference plane. Therefore, the same point "N" in the projected image will be recorded as the point "A" in the reference image (i.e., the image acquired without the test object on the test plate) and point "C" in the distorted image (i.e., the image acquired with the test object on the test plate). The distance between point "A" and point "C," $\overline{CA}$, represents the displacement of the same point "N" between the distorted and reference images.
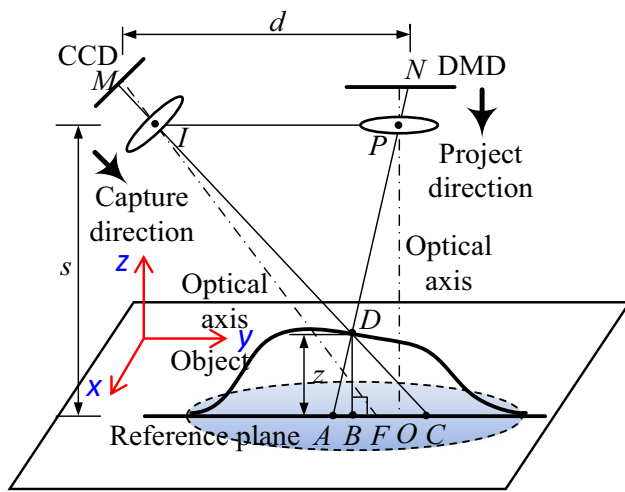
Fig. 2 Schematic diagram of the displacement to height conversion

Assume the distance between point "*M*" and point "*N*" is "*d*," and the reference plane is parallel to the device with a distance "*s*" between them. By analyzing the relationship between $\triangle MND$ and $\triangle CAD$, it can get:

$$\frac{d}{\overline{CA}} = \frac{s - \overline{BD}}{\overline{BD}} = \frac{s}{\overline{BD}} - 1 \tag{1}$$

Because the distance "*s*" is usually much larger than $\overline{BD}$, this equation can be simplified as:

$$Z(x,y) = \overline{BD} \approx \frac{s}{d}\overline{CA} = K\overline{CA} \tag{2}$$

It should be noted that, because the values of "*s*" and "*d*" are fixed for a given DIP system, *K* will be a constant for a given DIP system, which can be determined through a calibration procedure. Equation (2) shows a linear relationship between measured displacement $\overline{CA}$ and the object height

$Z(x, y)$. Therefore, the 3D shape of the test object can be determined quantitatively by measuring the displacements between the distorted and reference images at the points of interest.

2.2.2 A spatial cross-correlation algorithm for DIP measurements

In the present study, a spatial cross-correlation image processing algorithm is used in the analysis to determine the displacement vectors at the points of interest between the distorted and the reference images. It should be noted that spatial cross-correlation techniques have been not only widely used for the image processing of particle image velocimetry (PIV) measurements (Adrian 1991, 2005; Raffel et al. 1998), but also successfully applied for molecular tagging velocimetry (MTV) measurements (Hu and Koochesfahani 2006, 2011; Hu et al. 2010). The spatial cross-correlation algorithm developed by Gendrich and Koochesfahani (1996) is particularly suitable for the image processing of DIP measurements.

Figure 3 shows the schematic of the spatial cross-correlation algorithm along with a typical DIP reference and distorted image pair. Here, we show a reference image with regular grid and the corresponding distorted image produced by a small spherical cap placed on the test plate. To implement the spatial cross-correlation algorithm, a small window (referred as the interrogation window) is selected in the reference image and is cross-correlated with a larger window in the distorted image, thus giving the correlation coefficients, $R(m, n)$, with the following formula:

$$R(m,n) = \frac{\sum_i \sum_j \left(I_r(i,j) - \overline{I_r}\right)\left(I(i+r,j+s) - \overline{I}\right)}{\sqrt{\sum_i \sum_j (I_r(i,j) - \overline{I_r})^2 \sum_i \sum_j (I(i+r,j+s) - \overline{I})^2}}$$

$$\tag{3}$$
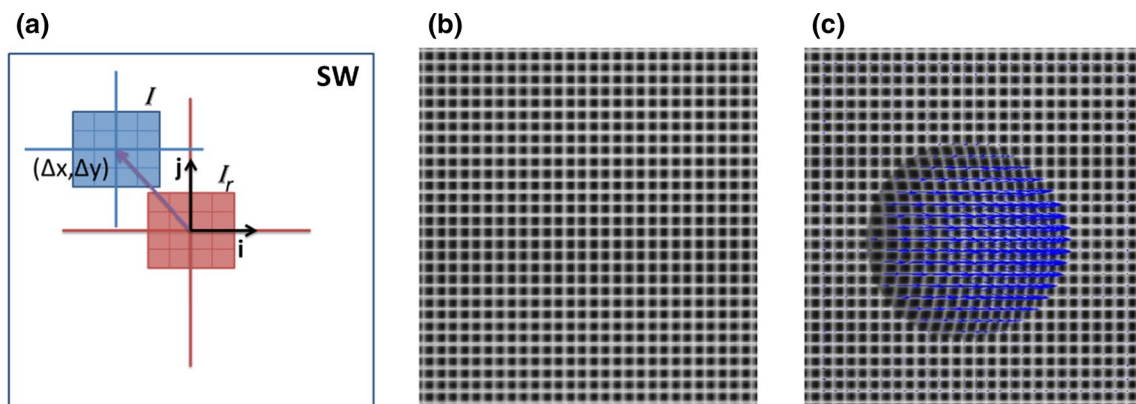
Fig. 3 Schematic of spatial cross-correlation algorithm and a pair of typical DIP images. **a** Spatial cross-correlation algorithm. **b** Reference image. **c** Distorted image with displacements

where I_r and I represent the image intensities of the interrogation windows taken from the reference image and distorted image, respectively. $\bar{I}_r$ and $\bar{I}$ are the corresponding mean intensity values. While i and j refer to the horizontal and vertical directions, (r, s) is the searching vector. As described in Gendrich et al. (1997), the displacement vector $(\Delta x, \Delta y)$ of the small interrogation window can be determined by finding the location of the peak correlation coefficient. Figure 3c shows the displacement vectors at the points of interest (i.e., at the cross-points of the grid image) between the reference image and the distorted image, which were determined by using the spatial cross-correlation algorithm described above. Following the work of Gendrich et al. (1997), the displacement vectors are located to sub-pixel accuracy by using a polynomial fit.
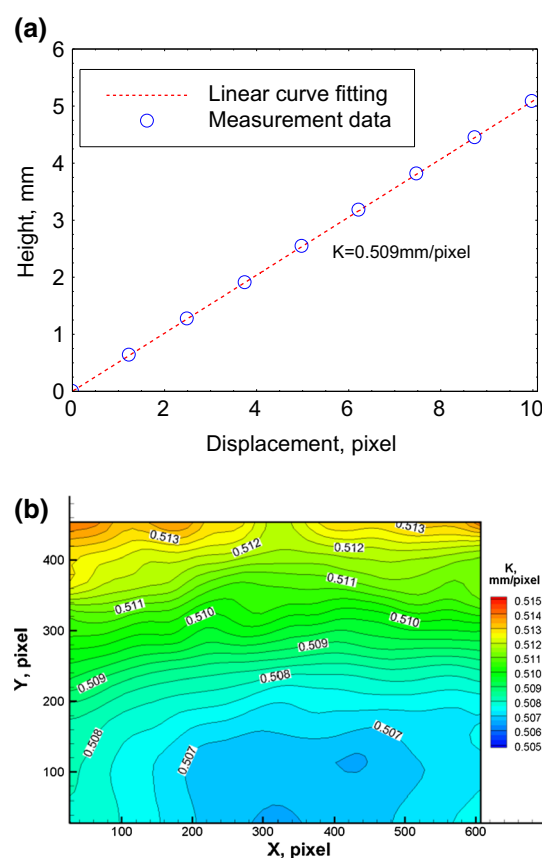
2.2.3 DIP calibration procedure

As shown in Eq. (2), for a given DIP system, the displacement of a corresponding point between the distorted and the reference images would change linearly with the object height $Z(x, y)$. A calibration procedure similar as that described in Hu et al. (2014) for the calibration of DFP measurements can be used to determine the displacement-to-height conversion constant "K" for the DIP measurements. Instead of projecting a digital fringe pattern onto a calibration plate for DFP calibration, a grid image is used for DIP calibration. A shown schematically in Fig. 4, a portable digital projector is used to project the grid image onto a calibration test plate (100 mm × 100 mm), which is located 1200 mm away from the projector. The test plate is mounted on the top of a vertical translation stage, and the height of the vertical translation stage (i.e., the position of the test plate along Z-direction) is adjusted with a micrometer drive with a resolution of 10 μm. A digital camera is used to acquire the images projected on the test plate. The acquired images are stored on the host computer for image processing.

For the DIP calibration, the test plate is moved to 10 parallel positions in Z-direction at an interval of 0.5 mm by adjusting the height of the vertical translation stage. The projected grid image on the test plate is acquired at each pre-determined position. Then, the images are processed by using the spatial cross-correlation algorithm described above to calculate the displacement vectors of the acquired grid images in reference to the image acquired with the test plate at the origin position of $Z = 0$. Figure 5a shows the derived displacements at the center of the measurement window as the test plate is moved away from its original position. Clearly, the relationship between the height and the image displacement at the point of interest can be
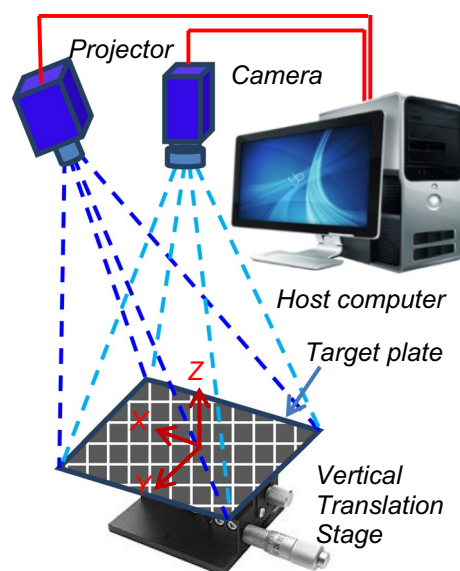
Fig. 4 Setup for DIP calibration

Fig. 5 The displacement-to-height factor obtained by a DIP calibration procedure. **a** Height versus displacement profile at the center of the measurement window. **b** The displacement-to-height factor distribution in the measurement window

fitted well by a linear function, as predicted theoretically by Eq. (2). The linear scale factor derived from calibration procedure is used for the displacement to height conversion of the DIP measurements. It should also be noted that Eq. (2) suggests that the displacement-to-height conversion factor would be a constant over the whole measurement window for a given DIP configuration. The measured values of the displacement-to-height conversion factor given in Fig. 5b confirm that the variations of the displacement-to-height conversion factor over the entire measurement window are smaller than 3.0 %, which accounts for all the alignment imperfections of the camera and projector and the distortions of the optics and camera lenses used for the DIP measurements.

2.3 On the resolution limitations and uncertainty levels of the DIP measurements

The present DIP technique, like most image correlation-based measurement techniques, does not give information at a "point." Rather, it provides the spatially averaged measurement of a region. Similar to PIV and MTV, the effective spatial resolution of DIP measurements is given by the sum of the interrogation window size used for the cross-correlation calculation and the measured displacement vector between the deformed and reference images. Clearly, it would require projected grid image and selecting interrogation windows consistent with the scales to be resolved in order to obtain resolved data to measure the small-scale structures. While the best spatial resolution would be set by the width of the projected images lines used to generate the grid pattern and the resolution characteristics of image detection, the selection of the interrogation window would often involve a choice between the spatial resolution and the accuracy levels of the DIP measurements. The temporal resolution of the DIP measurements would be determined by the exposure time used to acquire the DIP images. For the DIP measurement results given in the present study, the spatial resolution of the DIP measurements was dominated by the final source window size of 7×7 pixels for the cross-correlation calculation, which is about 1.0 mm $\times$ 1.0 mm in physical space.

The accuracy of DIP measurements may be affected by many factors, which include the important parameters for DIP system setup such as the angle between the projector and camera; the distance between projector, camera, and object; and the resolution of the projector and camera. The signal-to-noise ratio in the acquired DIP images, the intersection angle and width of the projected grid lines, and the size of the source window used for the correlation process may also affect the uncertainty of the DIP measurements. With similar grid images as those used in the present study, Gendrich and Koochesfahani (1996) studied the effects of

such factors systematically and found that the uncertainty in the measurement of the displacement of grid images in the correlation process is given by a 95 % confidence limit of about ± 0.2 pixel, or an rms accuracy of ± 0.1 pixel, assuming a Gaussian distribution for error. Considering a maximum displacement of 5 pixels between the distorted images and reference image in the DIP measurements given in the present study, the sub-pixel accuracy in the correlation calculation is about 2.0 %. It should also be noted that the resolution of the translation stage used for the DIP calibration procedure may also affect the uncertainty levels of the DIP measurements, which would contribute to a system error in DIP measurements.

3 Application of DIP to measure the 3D shape of a spherical cap

In order to demonstrate the implementation and feasibility of the DIP technique described above, a DIP system was used to measure the 3D shape (i.e., thickness distribution) of a small spherical cap placed over a test plate. The nominal dimensions of the spherical cap are given schematically in Fig. 6a; specifically, the height of the spherical cap is $H = 4.00$ mm and the base diameter is $D = 20.00$ mm. The acquired reference image and a distorted image with the spherical cap present on the test plate are shown in Fig. 3b, c, respectively. As described above, a spatial cross-correlation algorithm was used to calculate the displacement vectors at the points of interest (i.e., at the cross-points of the grid image) between the acquired reference and the distorted images. Using the phase-to-height conversion factor as that shown in Fig. 5b, the thickness distribution of the spherical cap can be determined based on the displacement vectors shown in Fig. 3c. The DIP measurement result in terms of the height distribution of the spherical cap is given in Fig. 6b. Since the nominal height distribution of the spherical cap was known, the measurement accuracy of the DIP system can be evaluated by comparing the measured height distribution with the nominal shape of the spherical cap quantitatively. The distribution of the DIP measurement errors is presented in Fig. 6c.

It can be seen clearly that DIP measurement uncertainty is relatively high in the region near the base of the spherical cap. The relatively larger uncertainty may result from the rather rapid changes of the height at the base, as well as relatively poor spatial resolution of projected grids in the region. Since the optimal projected grid pattern must ensure both a high spatial resolution and good image quality (and such issues may conflict), a comprehensive study is needed to evaluate the sensitivity of the important parameters of a DIP system configuration: such as the gap and orientations of the projected grids; the angle between the projector and
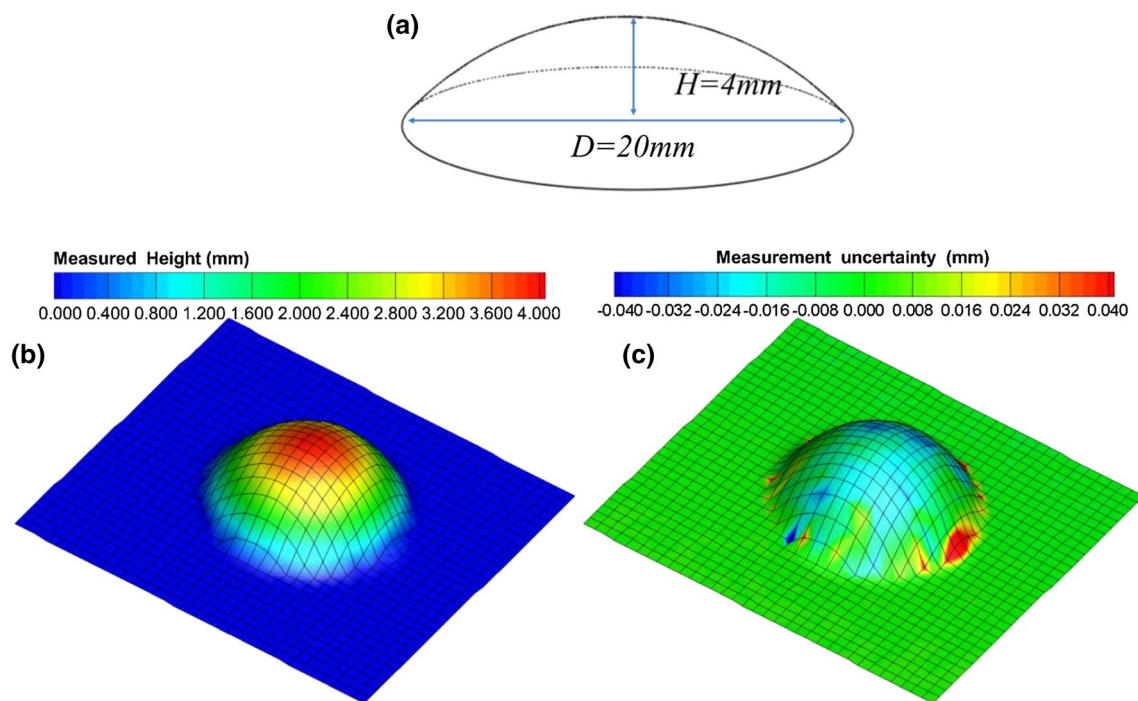
Fig. 6 DIP measurement of a spherical cap on a test plate. **a** The dimensions of the spherical cap. **b** DIP measurement results. **c** Measurement error distribution

camera; the distance between projector, camera, and object; and the resolution of the projector and camera versus the size the measurement window. With the DIP system setup used in the present study for the spherical cap measurements, the measurement uncertainty level was found to be about 0.02 mm, which is about 0.5 % of the nominal height of $H = 4.00$ mm. This is the total uncertainty and accounts for all the effects discussed above.

It should be noted that the DFP technique described in Hu et al. (2014) was also used to measure the 3D profile of the spherical cap as given in Fig. 6. A side-by-side comparison of the measurement results of the spherical cap by using DIP and DFP technique was given in Zhang et al. (2013), which reveals that the DIP technique can reduce the measurement error by a factor of 3, in comparison with the DFP technique described in Hu et al. (2014).

4 Quantification of the surface water transport process over a NACA0012 airfoil

In the present study, the DIP technique was used to quantify the surface water transport process over a NACA0012 airfoil driven by boundary layer airflows. It should be noted that, while a number of theoretical and numerical studies have been conducted in the past years to investigate the water runback process over airfoil surfaces (Nelson et al. 1995;

Thompson and Jang 1996; Thompson and Marrochello 1999; Tsao et al. 1997; Rothmayer et al. 2002; Da Silveira 2003; Ueno and Farzaneh 2011; Rothmayer and Hu 2012, 2013), very little can be found in the literature to provide quantitative measurements to evaluate the theoretical models and scaling laws pertinent to water runback processes over airfoil surfaces (Olsen and Walker 1987). To the best knowledge of the authors, the experimental work described in the present study is believed to be the first to provide quantitative, whole-field DIP measurement results to reveal the transient behavior of the water runback process over an airfoil surface.

4.1 Experimental setup and test model

The experimental study was performed in the Iowa State University Icing Research Tunnel (ISU-IRT) in the Aerospace Engineering Department of Iowa State University. The ISU-IRT, which was recently donated by UTC Aerospace System (formerly Goodrich Corporation) to Iowa State University, is a newly refurbished research-grade multifunctional icing research tunnel. It has a test section of 10×10 inches^2 (254×254 mm^2) in cross section, and the walls of the test section are optically transparent. It has a capacity of generating a maximum wind speed of 100 m/s and airflow temperature of -30 °C. The turbulence level of the oncoming airflow at the entrance of the test section is about 3.0 % as measured by a hot wire anemometer. An array of pneumatic atomizing

spray nozzles is installed at the entrance of the contraction to inject micro-sized water droplets (10–50 μm in size) into the airflow. By adjusting the water flow rate thorough the spray nozzles, the liquid water content (LWC) in the tunnel could be set; thus, the ISU-IRT can be run over a range of test conditions to duplicate various atmospheric icing phenomena (e.g., from rime ice to extremely wet glaze ice conditions). In the present study, deionized water was employed as the working liquid injected into the airflow through the spray nozzles. Following the work of Cobelli et al. (2009), a small amount of white latex paint was added into the water to enhance the contrast of the projected images on the free surface of the water film/rivulet flows. In the present study, the flow rate of the water through the spray system was fixed at $Q = 800$ ml/min during the experiments such that the corresponding LWC in the test section was $LWC \approx 7.0$–21.0 g/m^3 as the oncoming airflow velocity varied from $V_\infty = 30$ m/s to $V_\infty = 10$ m/s.

Figure 7 shows the schematic of the experimental setup used in the present study to use DIP technique to quantify wind-driven surface water transport process over an airfoil. As shown in the figure, a NACA0012 airfoil with a chord length $C = 101$ mm was installed in the center of the test section. The airfoil was 3D printed by using a rapid prototyping machine. The surfaces of the airfoil were carefully polished and then coated with flat white paint to improve the diffuse reflectivity of the projected grid images on the airfoil. The airfoil was mounted at a zero angle of attack in relation to the oncoming airflow ($\alpha = 0.0$ °). Because the main focus of the

present study is to demonstrate the feasibility and implementation of the DIP technique to quantify the transient behavior of the wind-driven surface water transport processes on an airfoil, the air temperature inside the ISU-IRT was kept at room temperature ($T_\infty = 20$ °C). The velocity of the oncoming airflow in the test section was adjusted from $V_\infty = 10$ m/s to $V_\infty = 30$ m/s. Consequently, the corresponding Reynolds numbers based on the chord length of the airfoil and the airflow velocity varied from $Re = 0.67 \times 10^5$ to 2.0×10^5.

As shown in Fig. 7, a projector (Dell DLP-M109S, 858×600 pixels^2 in resolution) was used to project a grid image onto the surface of the airfoil for the DIP measurements. A progressive scan CCD camera (Imaging Source Corp. DMKBU2104 with 640×480 pixels^2 in resolution) with a Pentax C1614-M lens was used for the DIP image acquisition. The digital camera and the projector were synchronized with a digital delay generator (BNC Model 575-8C). The frame rate of the digital camera for DIP image acquisition was set to 30 Hz with 2.0-ms exposure time. For each tested case, 1200 images (i.e., 60 s in duration) were recorded after the spray nozzles were turned on to inject water droplets into the airflow. Figure 8 shows a reference image and a typical deformed image modulated by water film and rivulet flows, along with the corresponding DIP measurement of the thickness distribution of the water film and rivulet flows over the airfoil. Because the rectangular grid image was projected onto the curved surface of the NACA0012 airfoil, the straight lines of the grids

Fig. 7 Experimental setup used to quantify surface water runback over an airfoil
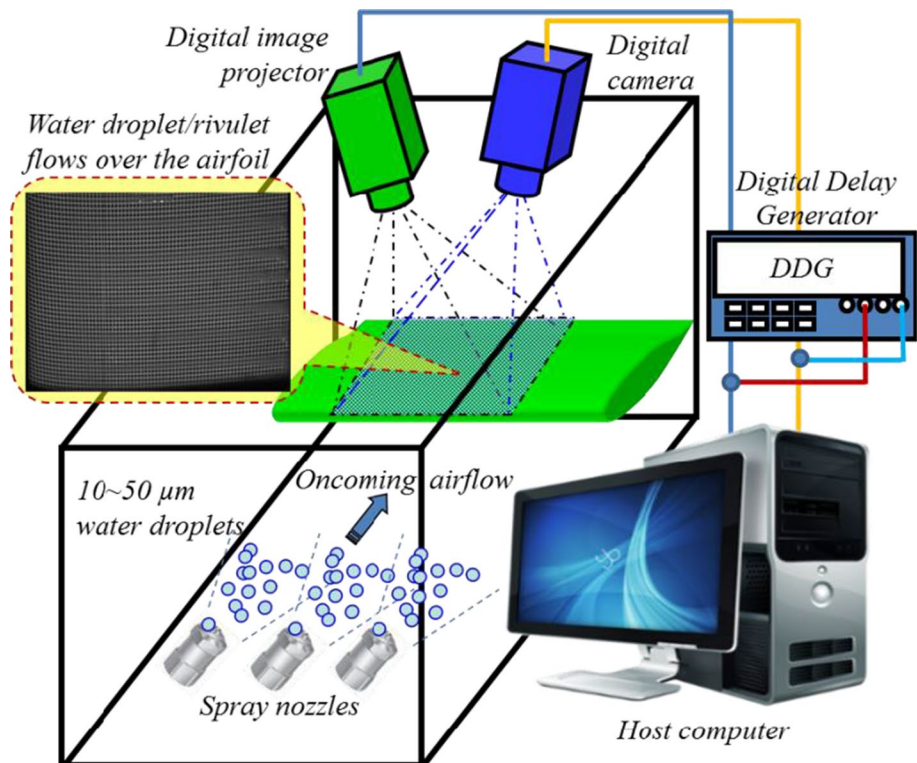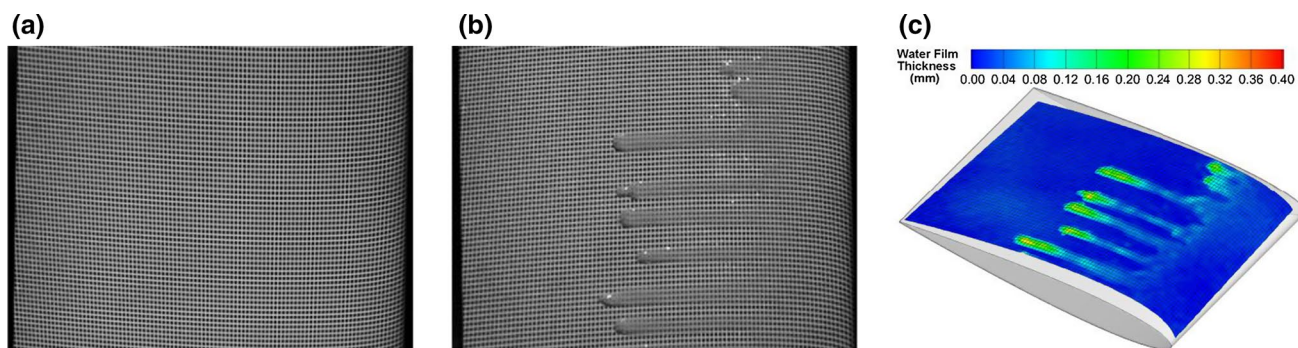
Fig. 8 Typical acquired DIP images and corresponding measurement result to quantify the surface water transport process over the NACA0012 airfoil. **a** Reference image. **b** Modulated image with film/rivulet flows. **c** DIP measurement result
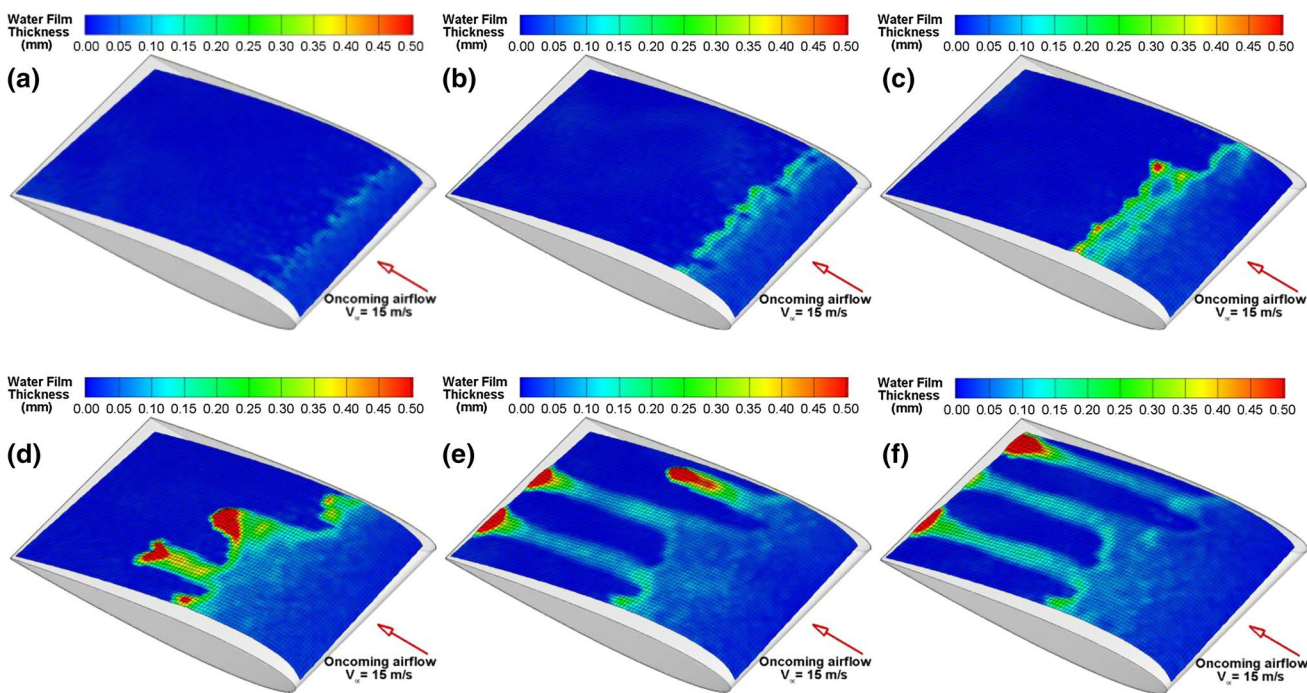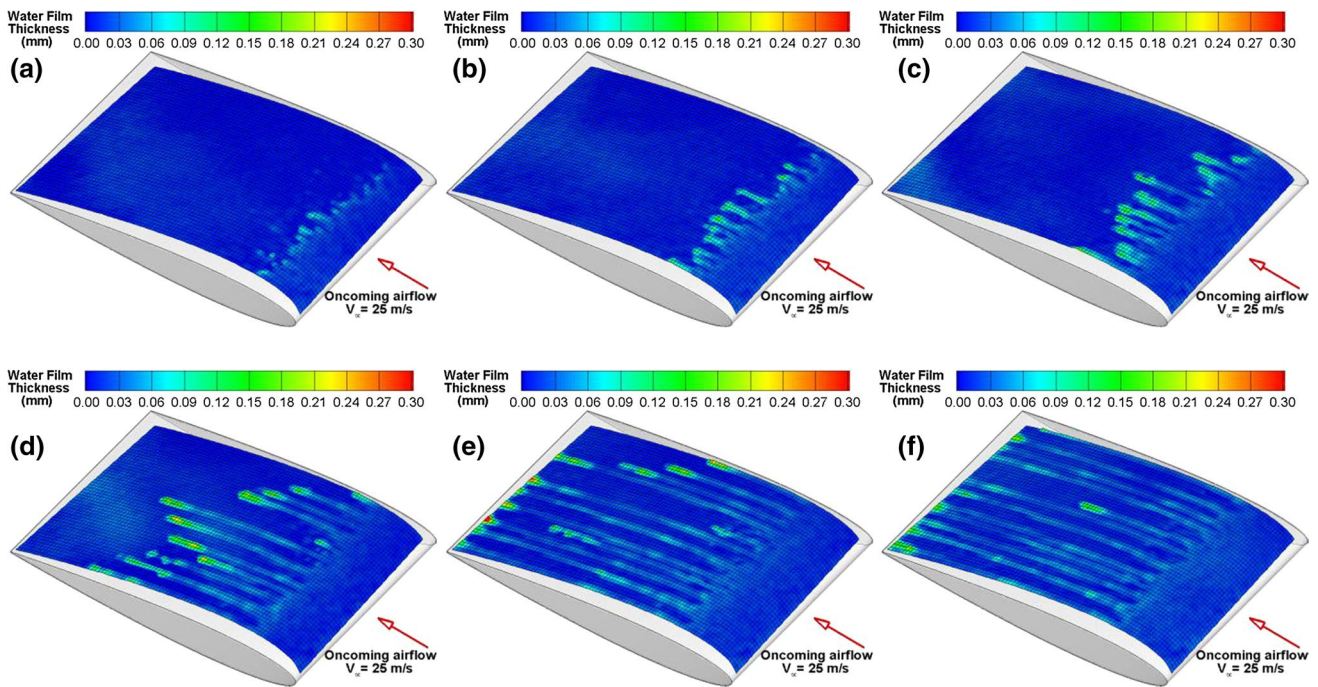

Fig. 9 Time evolution of the surface water film/rivulet flows over the airfoil surface with the oncoming airflow velocity $V_\infty = 15$ m/s. **a** $t = t_O + 1.0$ s. **b** $t = t_O + 2.0$ s. **c** $t = t_O + 4.0$ s. **d** $t = t_O + 6.0$ s. **e** $t = t_O + 9.0$ s. **f** $t = t_O + 12.0$ s

became curved lines in the reference image, as shown in Fig. 8a. It can also be seen that, in comparison with the reference image, the grid patterns in the acquired DIP image (Fig. 8b) were substantially deformed by the existence of water film and rivulet flow on the airfoil. Figure 8c shows the corresponding DIP measured thickness distribution of the water film and rivulet flows over the airfoil surface.

4.2 To quantify the unsteady water transport process over an airfoil surface

Figures 9 and 10 present typical DIP measurement results, revealing the time evolution of the surface water transport

process over the surface of the airfoil with the freestream velocities of the oncoming airflow at $V_\infty = 15$ m/s and $V_\infty = 25$ m/s, respectively. As shown in Figs. 9a and 10a, the water droplets carried by the oncoming airflow impinge onto the airfoil surface mainly in the region near the leading edge of the NACA0012 airfoil, specifically, within the first 5 % of the chord length, which confirmed the findings of the numerical simulation study of Da Silveira (2003). After collecting on the airfoil and driven by the boundary layer airflow over the airfoil, the water runs back along the airfoil surface. Figures 9b and 10b reveal that the water droplets coalesced to form a thin water film over the airfoil surface as they runback. The front contact line of the

Fig. 10 Time evolution of the surface water film/rivulet flows over the airfoil surface with the oncoming airflow velocity $V_\infty = 25$ m/s. **a** $t = t_O + 0.2$ s. **b** $t = t_O + 0.50$ s. **c** $t = t_O + 1.0$ s. **d** $t = t_O + 2.0$ s. **e** $t = t_O + 3.0$ s. **f** $t = t_O + 4.0$ s

water film bulged and formed isolated water rivulets further downstream, which is seen in Figs. 9c and 10c. As shown in Figs. 9d, e and 10d, e, with continuous forcing by the airflow over the airfoil, the front lobes of the water rivulets ran back very quickly along the airfoil surface and were subsequently shed from the trailing edge. As a result, several isolated water transport channels were found to be formed along the moving paths of the water rivulet flows over the airfoil surface, as shown in Figs. 9f and 10f. It should be noted that, after the water transport channels formed on the airfoil surface, the surface water transport process settled into a steady state. No further changes were observed in the water transport pattern on the airfoil surface. The water flow along the water channels was responsible for transporting all the surface water mass subsequently accumulated in the impingement region of the wing. Olsen and Walker (1987) also observed similar phenomena in their experimental study to investigate the surface water transport process over an airfoil surface at above freezing temperature condition.

Based on the comparison of the time evolution of the surface water film/rivulet flows over the airfoil surface given in Figs. 9 and 10, it can be seen that the transition of the surface water transport process from a water film flow into rivulet flows occurs much further upstream as the oncoming airflow velocity increases. The runback speed of the front lobes of the rivulets was also found to increase rapidly as the oncoming airflow velocity increases. For

the case with the oncoming airflow velocity $V_\infty = 15$ m/s, the runback speed of the rivulet flows was about $V_{\text{runback}} = 0.013$ m/s. In comparison, the rivulet runback speed increased to $V_{\text{runback}} = 0.035$ m/s with the oncoming airflow velocity increased to $V_\infty = 25$ m/s, an increase of about three times.

After the surface water transport process over the airfoil surface reached a steady state, 600 frames of the instantaneous DIP measurement results (i.e., obtained within a time duration of 20 s) were used to determine the time-averaged film thickness distributions of the surface water film/rivulet flows over the airfoil. Figure 11 gives the time-averaged water film thickness distribution over the airfoil with the freestream velocity of the oncoming airflow increasing from $V_\infty = 10$ m/s to $V_\infty = 25$ m/s. Both the rivulet widths and the gaps between neighboring rivulets became smaller with increasing velocity of the oncoming airflow.

Based on the time-averaged water film thickness distributions at the test conditions shown in Fig. 11, the film thickness profiles along the centerline of the water transport channels (i.e., within the streamwise cross section of the water rivulets as indicated in Fig. 11a, b) were extracted for a more quantitative comparison of the surface water transportation process between the different test cases. Figure 12 gives the extracted water film thickness profiles along the centerlines of the water transport channels as the velocity of the oncoming airflow increases from $V_\infty = 10$ to 25 m/s. The transition locations of the surface water transport from

Fig. 11 Time-averaged water film thickness distribution over the airfoil. **a** Oncoming airflow velocity $V_\infty = 10$ m/s. **b** Oncoming airflow velocity $V_\infty = 15$ m/s. **c** Oncoming airflow velocity $V_\infty = 20$ m/s. **d** Oncoming airflow velocity $V_\infty = 25$ m/s
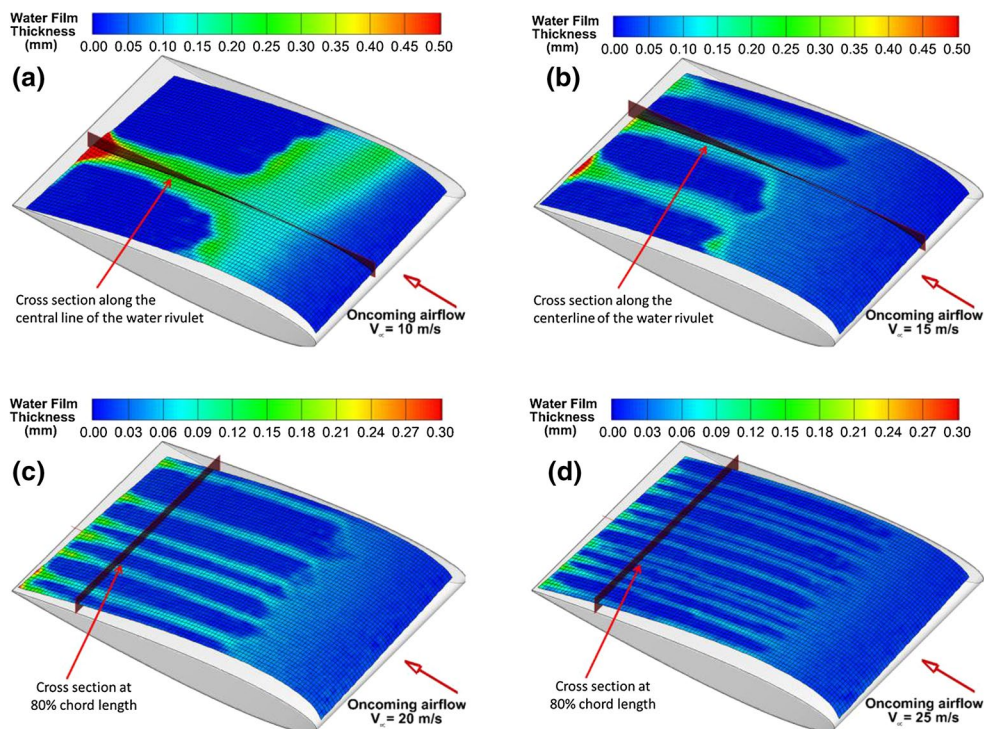

film flows to rivulet flows at the different test conditions are listed in Table 1 and are also indicated in the plots for comparison.

As shown in Fig. 12, the location of the surface water transport transition from film flows to rivulet flows moved further upstream toward the leading edge as the oncoming airflow velocity increased. While the film flow covered more than the front 50 % of the airfoil surface when $V_\infty = 10$ m/s f (i.e., up to $X/C = 0.515$), the film flow ended at the downstream location of $X/C = 0.252$ when the oncoming airflow velocity increased to $V_\infty = 30$ m/s. The measurement results given in Fig. 12 also reveal that, as the surface water advanced along the airfoil, the thickness of the water film/rivulet flows increased monotonically for all of the test cases.

Figure 13 presents the transverse profiles of the averaged water film thickness in the spanwise cross section at $X/C = 0.80$ downstream location (i.e., within the spanwise cross section shown in Fig. 11c, d) for freestream velocities of the oncoming airflow increased from $V_\infty = 10$ m/s through $V_\infty = 30$ m/s. Based on the measurement data shown in Fig. 13, the averaged width of the rivulets (i.e., the water transport channels) as well as the average gap between neighboring water rivulets can be determined quantitatively, and the measurement results are listed in Table 1. The measurements given in Table 1 reveal that the width of the rivulets and the gap between the neighboring water transport channels decrease rapidly with the increasing freestream velocity of the oncoming airflow. While

the averaged width of the rivulet flows was about 14 % of the airfoil chord length for $V_\infty = 10$ m/s, the rivulet width decreased to less than 2 % of the airfoil chord as the oncoming airflow velocity increased to $V_\infty = 30$ m/s. The rivulet width decreased by a factor of 7 when the airflow velocity was increased three times. Correspondingly, the gap between the neighboring water rivulets also decreased from greater than 35 % of the airfoil chord for when $V_\infty = 10$ m/s to only about 5 % of the airfoil cord when $V_\infty = 30$ m/s. This indicates that the averaged gap between the neighboring rivulets also became about seven times smaller for a factor-of-three increase in the freestream velocity of the oncoming airflow.

Based on the comparison of the measurements at different test conditions as shown in Fig. 13, it can also be seen that, while the flow rate of the liquid water added to the airflow was fixed during the experiments, the thickness of the water film/rivulet flows over the airfoil decreased rapidly as the freestream velocity of the oncoming airflow increased. Figure 14 presents the variations of the measured water film/rivulet thickness data at the same point of interest on the airfoil surface (i.e., on the centerlines of the water transport channels at the downstream location of $X/C = 0.80$) as a function of the oncoming airfoil velocity, which reveals the effects of the oncoming airflow velocity on the thickness of the water film/rivulet flows over the airfoil surface more clearly and quantitatively. As shown in Fig. 14, the relationship between the measured film thickness data at the compared point and the freestream velocity
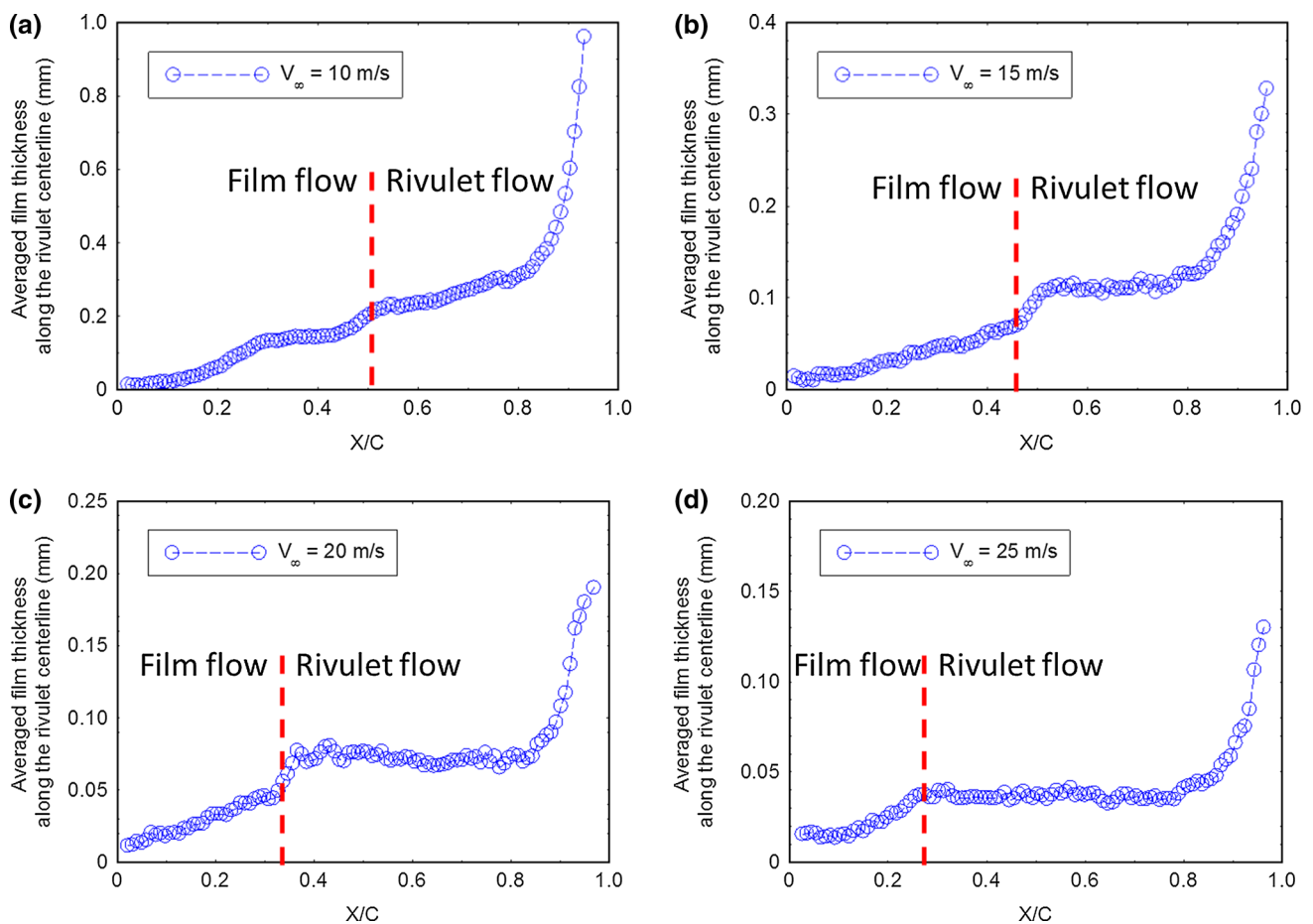
Fig. 12 Averaged water film thickness along the rivulet centerline at different test conditions. **a** Oncoming airflow velocity $V_\infty = 10$ m/s. **b** Oncoming airflow velocity $V_\infty = 15$ m/s. **c** Oncoming airflow velocity $V_\infty = 20$ m/s. **d** Oncoming airflow velocity $V_\infty = 25$ m/s

| **Table 1** A list of the transition locations, averaged widths of the rivulets, and averaged gap between the rivulets at different test conditions	Velocity of the oncoming airflow (m/s)	Transition location from film flows to rivulet flows (% airfoil chord length)	Averaged width of the rivulet flows (% airfoil chord length)	Averaged gap between the rivulet flows (% airfoil chord length)
	10.0	51.5	13.64	>35
	15.0	44.2	9.51	17.41
	20.0	35.3	4.92	10.23
	25.0	27.1	3.03	6.34
	30.0	25.2	1.97	5.19

of the oncoming airflow can be fitted well by a power function with the power-law exponent being about 2.0. This power-law relationship suggests that the thickness of the water film/rivulet flows over the airfoil surface decreases rapidly with increasing freestream velocity of the oncoming airflow; namely, the thickness of the water film/rivulet flows over the airfoil surface is approximately proportional to the reciprocal of the velocity squared of the oncoming airflow.

5 Conclusions

In the present study, an experimental study was conducted to characterize the transient behavior of the surface water film/rivulet flows driven by the airflows over a NACA0012 airfoil in order to elucidate the underlying physics of the surface water transport process pertinent to aircraft icing phenomena. A DIP technique was developed and applied to achieve quantitative measurements of the thickness
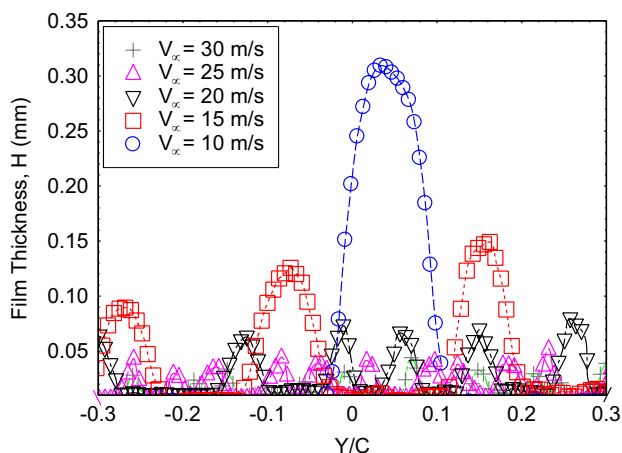
Fig. 13 Transverse profiles of the water film thickness in the spanwise cross section at $X/C = 0.80$ downstream location for different test conditions
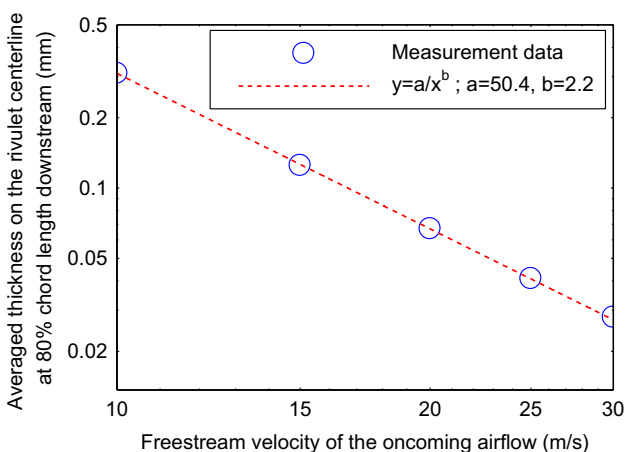
Fig. 14 Averaged thickness of the rivulet flows versus the oncoming airflow velocity

distribution of the water film/rivulet flows spreading over the surface of an airfoil. The DIP technique is based on the principle of structured light triangulation in a fashion similar to stereo vision technique, but replaces one of the cameras in the stereo pair with a digital projector. A grid image with known pattern characteristics was projected onto the test object of interest (i.e., water film/rivulet flows over an airfoil surface for the present study). Due to the complex three-dimensional (3D) geometrical profiles of the test objects (i.e., the free surfaces of the water film/rivulet flows), the projected grid patterns are deformed when observed from a perspective different from the projection axis. By comparing the distorted grid patterns (i.e., acquired images with water film/rivulet flows over the airfoil surface) with a reference grid pattern without the test objects on a reference surface, the 3D profile of the test

objects (i.e., the thickness distribution of the water film/rivulet flows, thus the surface water mass transport process) can be retrieved quantitatively and instantaneously. The feasibility and implementation of the DIP technique were first demonstrated by measuring the 3D shape of a small spherical cap placed on a flat test plate. The DIP measurement results were compared with the nominal height distribution of the spherical cap to evaluate the measurement uncertainty of the DIP system. With the parameter settings used in the present study, the measurement uncertainty level of the DIP system was found to be less than 0.5 % of the nominal height of the spherical cap.

After carefully calibrated and validated, the DIP technique was utilized to quantify the wind-driven surface water transport processes over a NACA0012 airfoil. The dynamic runback motion of the water film/rivulet flows driven by the boundary layer airflows over the airfoil surface was measured quantitatively and in real time from the time-resolved DIP measurements. It was found that micro-sized water droplets carried by the oncoming airflow impinged onto the airfoil surface, mainly in the region near the leading edge of the airfoil/wing model (i.e., within the first 5 % of the airfoil chord length). After impinging onto the airfoil, the water droplets coalesced as they ran back, resulting in the formation of thin water film flow over the front surface of the airfoil. As the film moved downstream, the front contact line of the film flows began to bugle locally at first and then formed isolated water rivulets further downstream. Driven by the boundary layer airflow over the airfoil surface, the front lobes of the rivulets quickly ran back and were shed from the airfoil trailing edge. As a result, several isolated water transport channels formed along the moving paths of the water rivulets over the airfoil surface. The surface water transport process over the airfoil surface reached steady state after the water rivulets shed from the airfoil trailing edge. The water flows through the water channels were found to be responsible for transporting the water mass collected at the leading edge from the continuous impingement of the water droplets carried by the oncoming airflow.

The DIP measurement results also reveal quantitatively that, as the oncoming airflow velocity increased, the transition location of the surface water transport process from film flows to rivulet flows occurred much earlier and closer to the airfoil leading edge. As the surface water ran back along the airfoil surface, the thickness of the water film/rivulet flows increased monotonically with the increasing distance away from the airfoil leading edge. While the runback velocity of the rivulet flows increased rapidly with the increasing velocity of the oncoming airflow, the width of the rivulets and the gap between neighboring rivulets decreased. It was also found that the thickness of the water film/rivulet flows at the same downstream location over the

airfoil surface would decrease according to a power function of the oncoming airflow velocity.

The large amount of information gathered about the characteristics of the unsteady water film/rivulet flows driven by boundary layer airflows over the NACA0012 airfoil with respect to space and time is very useful to elucidate underlying physics to improve our understanding about the important micro-physical processes pertinent to ice formation and accretion over aircraft wings in atmospheric icing conditions. The quantitative measurement data obtained through the experimental studies such as this can also be used to create a comprehensive database to validate and/or verify current ice accretion models for more accurate prediction of glaze ice formation and accretion process and the water runback over thermally protected surfaces on aircraft wings. The new findings derived from the present study can also be used as a good starting point toward the development of effective and robust anti-/de-icing strategies tailored for aircraft icing applications.

References

Adrian RJ (1991) Particle-imaging techniques for experimental fluid mechanics. Annu Rev Fluid Mech 23:261–304

Adrian RJ (2005) Twenty years of particle image velocimetry. Exp Fluids 39:159–169

Benetazzo A (2006) Measurements of short water waves using stereo matched image sequences. Coast Eng 53(12):1013–1032

Bragg M, Gregorek G, Lee J (1986) Airfoil aerodynamics in icing conditions. J Aircr 23(1):76–81

Brakel TW, Charpin JPF, Myers TG (2007) One-dimensional ice growth due to incoming supercooled droplets impacting on a thin conducting substrate. Int J Heat Mass Transf 50:1694–1705

Cazabat AM, Heslot F, Troian SM, Carles P (1990) Fingering instability of thin spreading films driven by temperature gradients. Nature 346:824–826

Chinnov E, Kharlamov S, Saprykina A, Zhukovskaya O (2007) Measuring deformations of the heated liquid film by the fluorescence method. Thermophys Aeromech 14(2):241–246

Cobelli PJ, Maurel A, Pagneux V, Petitjeans P (2009) Global measurement of water waves by Fourier transform profilometry. Exp Fluids 46:1037–1047

Cochard S, Ancey C (2008) Tracking the free surface of time-dependent flows: image processing for the dam-break problem. Exp Fluids 44:59–71

Da Silveira, RA, Maliska CR, Estivam DA, Mendes R (2003) Evaluation of collection efficiency methods for icing analysis. In: Proceedings of 17th international congress of mechanical engineering, Sao Paulo

Gendrich CP, Koochesfahani MM (1996) A spatial correlation technique for estimating velocity fields using Molecular Tagging Velocimetry (MTV). Exp Fluids 22(1):67–77

Gendrich CP, Koochesfahani MM, Nocera DG (1997) Molecular tagging velocimetry and other novel applications of a new phosphorescent supramolecule. Exp Fluids 23(5):361–372

Gent RW, Dart NP, Cansdale JT (2000) Aircraft icing. Philos Trans R Soc Lond A 358:2873–2911

Hansman RJ, Turnock SR (1989) Investigation of surface water behavior during glaze ice accretion. J Aircr 26(2):140–147

Hu H, Huang D (2009) Simultaneous measurements of droplet size and transient temperature within surface water droplets. AIAA J 47(4):813–820

Hu H, Jin Z (2010) An icing physics study by using lifetime-based molecular tagging thermometry technique. Int J Multiph Flow 36(8):672–681

Hu H, Koochesfahani MM (2006) Molecular tagging velocimetry and thermometry and its application to the wake of a heated circular cylinder. Meas Sci Technol 17:1269–1281

Hu H, Koochesfahani MM (2011) Thermal effects on the wake of a heated circular cylinder operating in mixed convection regime. J Fluid Mech 685:235–270

Hu H, Jin Z, Nocera D, Lum C, Koochesfahani MM (2010) Experimental investigation of micro-scale flow and heat transfer phenomena by using molecular tagging techniques. Meas Sci Technol 21:085401

Hu H, Wang B, Zhang K, Lohry W, Zhang S (2014) Quantification of transient behavior of wind-driven surface droplet/rivulet flows by using a digital fringe projection technique. J Vis. doi:10.1007/s12650-014-0264-8

Johnson MFG, Schluter RA, Bankoff SG (1997) Fluorescent imaging system for global measurement of liquid film thickness and dynamic contact angle in free surface flows. Rev Sci Instrum 68(11):4097–4102

Johnson MFG, Schluter RA, Miksis MJ, Bankoff SG (1999) Experimental study of rivulet formation on an inclined plate by fluorescent imaging. J Fluid Mech 394:339–354

Kabov OA, Scheid B, Sharina IA, Legros J (2002) Heat transfer and rivulet structures formation in a falling thin liquid film locally heated. Int J Thermal Sci 41(7):664–672

Koomullila RP, Thompsona DS, Sonib BK (2003) Iced airfoil simulation using generalized grids. Appl Numer Math 46(3,4):319–330

Lel V, Al-Sibai F, Leefken A, Renz U (2005) Local thickness and wave velocity measurement of wavy films with a chromatic confocal imaging method and a fluorescence intensity technique. Exp Fluids 39(5):856–864

Liu J, Schneider JB, Gollub JP (1995) Three-dimensional instabilities of film flows Phys. Fluids 7(1):55–67

Mason J (1971) The physics of clouds. Oxford University Press, Oxford

Moisy F, Rabaud M, Salsac K (2007) Measurement by digital image correlation of the topography of a liquid interface 60th Annual Meeting of the Division of Fluid Dynamics, American Physical Society. Nov. 18–20:2007

Myers TG, Charpin JPF (2004) A mathematical model for atmospheric ice accretion and water flow on a cold surface Int. Int J Heat Mass Transf 47:5483–5500

Nelson JJ, Alving AE, Joseph DD (1995) Boundary layer flow of air over water on a flat plate. J Fluid Mech 284(1):159–169

Olsen W, Walker E (1987) Experimental evidence for modifying the current physical model for ice accretion on aircraft structures. In: NASA TM-87184, 1987

Otta SP, Rothmayer AP (2009) Instability of stagnation line icing. Comput Fluids 38(2):273–283

Politovich MK (1989) Aircraft icing caused by large supercooled droplets. J Appl Meteorol 28:856–868

Pouliquen O, Forterre Y (2002) Friction law for dense granular flow: application to the motion of a mass down a rough inclined plane. J Fluid Mech 453:133–151

Pringsheim P (1949) Fluorescence and phosphorescence. Interscience, New York

Raffel M, Willert CE, Kompenhans J (1998) Particle image velocimetry: a practical guide. Springer, New York

Rothmayer AP, Hu H (2012) Solutions for two-dimensional instabilities of ice surfaces uniformly wetted by thin films. In: 4th AIAA atmospheric and space environments meeting, New Orleans, 2012

Rothmayer AP, Hu H (2013) Linearized solutions of three-dimensional condensed layer films. In: 5th AIAA atmospheric and space environments conference, San Diego, 2013

Rothmayer AP, Matheis BD, Timoshin SN (2002) Thin liquid films flowing over external aerodynamics surfaces. J Eng Math 42(3–4):341–357

Salvi J, Fernandez S, Pribanic T, Llado L (2010) A state of the art in structured light patterns for surface profilometry. Pattern Recognit 43:2666–2680

Schagen A, Modigell M (2007) Local film thickness and temperature distribution measurement in wavy liquid films with a laser-induced luminescence technique. Exp Fluids 43:209–221

Thompson BE, Jang J (1996) Aerodynamic efficiency of wings in rain. J Aircr 33(6):1047–1053

Thompson BE, Marrochello MR (1999) Rivulet formation in surface-water flow on an airfoil in rain. AIAA J 37(1):45–49

Tsao JC, Rothmayer AP, Anatoly IR (1997) Stability of air flow past thin liquid films on airfoils. Comput Fluids 26(5):427–452

Tsubaki R, Fujita I (2005) Stereoscopic measurement of a fluctuating free surface with discontinuities. Meas Sci Technol 16(10):1894–1902

Ueno K, Farzaneh M (2011) Linear stability analysis of ice growth under supercooled water film driven by a laminar airflow. Phys Fluids 23:042103

Vargas M, Tsao JC (2007) Observations on the growth of roughness elements into icing feathers. In: AIAA paper no: AIAA-2007-0900, 45th AIAA aerospace sciences meeting and exhibit, Reno, January 8–11, 2007

Wright WB, Budakian R, Putterman SJ (1996) Diffusing light photography of fully developed isotropic ripple turbulence. Phys Rev Lett 76(24):4528–4531

Zhang Q, Su X (2002) An optical measurement of vortex shape at a free surface. Opt Laser Technol 34(2):107–113

Zhang X, Dabiri D, Gharib M (1996) Optical mapping of fluid density interfaces: concepts and implementations. Rev Sci Instrum 67(5):1858–1868

Zhang K, Zhang S, Rothmayer A, Hu H (2013) Development of a digital image projection technique to measure wind-driven water film flows. In: AIAA-2013-0247; 51st AIAA aerospace sciences meeting including the new horizons forum and aerospace exposition, Grapevine, 07–10 January 2013